International Journal of Nanomedicine

Dovepress
open access to scientific and medical research

Open Access Full Text Article

ORIGINAL RESEARCH

Multifunctional Near-Infrared Dye IR-817 Encapsulated in Albumin Nanoparticles for Enhanced Imaging and Photothermal Therapy in Melanoma

Jianv Wang[1,*], Hongye Liao[1,*], Jieming Ban[2], Sen Li[2], Xia Xiong[1], Qingqing He[1], Xinyu Shi[2], Hongping Shen[2], Sijin Yang[2], Changzhen Sun[2], Li Liu[1]

[1]Department of Dermatology, the Affiliated Hospital of Southwest Medical University, Luzhou, 646000, People's Republic of China; [2]Drug Research Center of Integrated Traditional Chinese and Western Medicine, National Traditional Chinese Medicine Clinical Research Base, the Affiliated Traditional Chinese Medicine Hospital of Southwest Medical University, Luzhou, 646000, People's Republic of China

*These authors contributed equally to this work

Correspondence: Changzhen Sun, Drug Research Center of Integrated Traditional Chinese and Western Medicine, National Traditional Chinese Medicine Clinical Research Base, the Affiliated Traditional Chinese Medicine Hospital of Southwest Medical University, Luzhou, 646000, People's Republic of China, Tel/Fax +86-136-9949-2406, Email sunchangzhen@swmu.edu.cn; Li Liu, Department of Dermatology, the Affiliated Hospital of Southwest Medical University, Luzhou, 646000, People's Republic of China, Tel/Fax +86-193-3860-9127, Email liuli@swmu.edu.cn

Background: Near-infrared cyanine dyes have high sensitivity and spatial resolution imaging capabilities, but they also have unavoidable drawbacks such as photobleaching, low water solubility, fluorescence quenching, and toxic side effects. As an effective biologic drug carrier, albumin combines with cyanine dyes to form albumin@dye nanoparticles. These nanoparticles can alleviate the aforementioned issues and are widely used in tumor imaging and photothermal therapy.

Methods: Herein, a newly synthesized near-infrared dye IR-817 was combined with bovine serum albumin (BSA) to create BSA@IR-817 nanoparticles. Through the detection of fluorescence emission and absorption, the optimal concentration and ratio of BSA and IR-817 were determined. Subsequently, dynamic light scattering (DLS) measurements and scanning electron microscopy (SEM) were used for the physical characterization of the BSA@IR-817 nanoparticles. Finally, in vitro and in vivo experiments were conducted to assess the fluorescence imaging and photothermal therapeutic potential of BSA@IR-817 nanoparticles.

Results: IR-817 was adsorbed onto the BSA carrier by covalent conjugation and supramolecular encapsulation, resulting in the formation of dispersed, homogeneous, and stable nanoparticles with a particle size range of 120–220 nm. BSA@IR-817 not only improved the poor water solubility, fluorescence quenching, and toxic side effects of IR-817 but also enhanced the absorption and fluorescence emission peaks in the near-infrared region, as well as the fluorescence in the visible spectrum. In addition, BSA@IR-817 combined with laser 808 irradiation was able to convert light energy into heat energy with temperatures exceeding 50 °C. By creating a mouse model of subcutaneous melanoma, it was discovered that the tumor inhibition rate of BSA@IR-817 was greater than 99% after laser irradiation and that it achieved nearly complete tumor ablation without causing significant toxicity.

Conclusion: Our research, therefore, proposes the use of safe and effective photothermal nanoparticles for the imaging, diagnosis, and treatment of melanoma, and offers a promising strategy for future biomedical applications.

Keywords: albumin, cyanine dyes, near-infrared imaging, photothermal therapy, melanoma

Introduction

Melanoma arises from the malignant transformation of melanocytes in the basal layer of the skin, accounting for ~5% of all skin cancers.[1] However, it is responsible for the majority of skin cancer-related deaths due to its high degree of malignancy and aggressive ability.[2] In recent years, numerous novel melanoma therapies have emerged, including targeted therapy (BRAF and MEK inhibitors) and immunotherapy (PD1/PDL1 inhibitors and CTLA4 inhibitors).[3–5] Nonetheless, due to the multiple drug

Received: 8 June 2023
Accepted: 21 August 2023
Published: 4 September 2023

resistance, as well as the inevitable toxic and side effects of drugs, which cause immune system damage, and organ function destruction, the overall prognosis of melanoma remains poor till date.[6–8] Thus, the effective treatment of melanoma still faces significant challenges, urging the development of new therapeutic approaches to alter the current melanoma treatment paradigm.

Photothermal therapy (PTT) has been widely used in the study of tumor therapy due to its fewer side effects, good controllability, and high selectivity.[9,10] It is an effective emerging strategy for cancer therapy that converts the energy of photothermal transduction agents (PTAs) into heat through the excitation of an external light source in order to induce the death of cancer cells.[11–13] Ideal PTAs have the following characteristics: First, long wavelengths in the near-infrared (NIR) range (>700 nm) and a high molar extinction coefficient are capable of producing an effective phototherapy effect.[14] Second, tumor targeting is crucial for enhancing the anticancer efficacy of PTAs. Due to their deep tissue penetration, weak background self-fluorescence, and low light scattering, NIR fluorescent dyes have attracted more and more interest in disease bioimaging diagnosis and treatment in recent years.[15–18] For instance, indocyanine green (ICG) is an NIR fluorescent probe approved by Food and Drug Administration (FDA) that has been utilized in tumor bioimaging.[19] In addition, cyanine dye-based NIR fluorescent probes (IR780, IR783, and IR808),[20–22] which are characterized by a hardened conjugated olefin in the cyclohexyl skeleton, wherein the conjugated olefin was replaced by meso-chlorine.[23] Chlorine-containing cyanine dyes have a longer residence time in tumor, greater optical stability, and a better fluorescence effect than non-chlorine-containing ICG.[24] As different chemical couplings can alter the structure of the targeted ligand, the fluorescence imaging ability, and the therapeutic potential.[25] We successfully synthesized IR-817, a new near-infrared fluorescent dye, by coupling IR-808 with dicyclohexylcarbodiimide in our previous study.[26] The in vitro and in vivo imaging studies revealed that IR-817 functioned as an excellent melanoma-targeting agent. In addition, IR-817 entered cells through organic anion-transporting polypeptides (OATPs), displaying structurally inherent tumor targeting. However, due to the disadvantages of IR-817, such as poor water solubility and a short imaging time, aggregation caused quench (ACQ) and acute toxicity (high dose). We need to find new ways to enhance IR-817 so that it has a greater potential for use in the diagnosis and treatment of cancer.

Albumin is biocompatible, non-toxic, easy to produce, and stable in vivo; consequently, it has been extensively utilized as a multifunctional drug delivery nanocarrier over the years.[27–29] There has also been reported that cyanine dyes can covalently bind to specific albumin domains in order to form albumin@dye nanoparticles, which can then be used for tumor imaging and photothermal therapy.[30–32] ICG can, for example, bind to albumin to prevent the aggregation of molecular dyes, thereby enhancing near-infrared fluorescence imaging.[33,34] IR-820, when combined with BSA, not only has good fluorescence imaging characteristics in the NIR region but it can also be used effectively for photoacoustic imaging.[35] In addition, IR-825 can effectively convert light energy into heat energy by binding with human serum albumin (HSA) to achieve photothermal ablation of tumors and kill cancer cells.[36] Through the interaction of covalent coupling and supramolecular encapsulation, these albumin@dye nanocomposites can not only prolong the drug release time but also aggregate at the tumor site via permeability and retention (EPR) effect in vivo.[37,38] In addition, under NIR laser radiation, stronger absorbance, greater fluorescence quantum yield, and improved photostability will be generated in order to achieve simultaneous tumor imaging and photothermal therapy.[39]

In this study, BSA bonded with IR-817 via covalent conjugation and supramolecular encapsulation to form BSA@IR-817 nanoparticles, which improved IR-817's poor water solubility, fluorescence quenching, tumor imaging, and toxic side effects. When irradiated using a NIR laser 808, BSA@IR-817 could achieve thermal ablation of tumors in vitro and in vivo while maintaining biosafety. Our research provides not only insights for the development, design, and application of nanoparticles for melanoma but also a concept for imaging guidance and photothermal therapy for melanoma (Scheme 1).

Materials and Methods

Materials and Chemicals

Indocyanine green (ICG), human serum albumin (HSA, ≥98%), bovine serum albumin (BSA, ≥98%) were purchased from Macklin Inc. (Shanghai, China), Dulbecco's modified Eagle's medium and fetal bovine serum (FBS) were purchased from BasalMedia (Shanghai, China), trypsin-EDTA, penicillin-streptomycin were supplied by Solarbio (Shanghai, China). 3-(4,5-diMethylthialzol-2-yl)-2,5-diphe-nyltetrazolium bromide (MTT) and Hoechst33342 were purchased from YuanYe Bio-Technology (Shanghai, China). The universal SP kit (mouse/rabbit streptavidin–biotin detection system), DAB kit and PBS buffer (pH 7.4) were purchased from Zsbio (Beijing, China). All-purpose

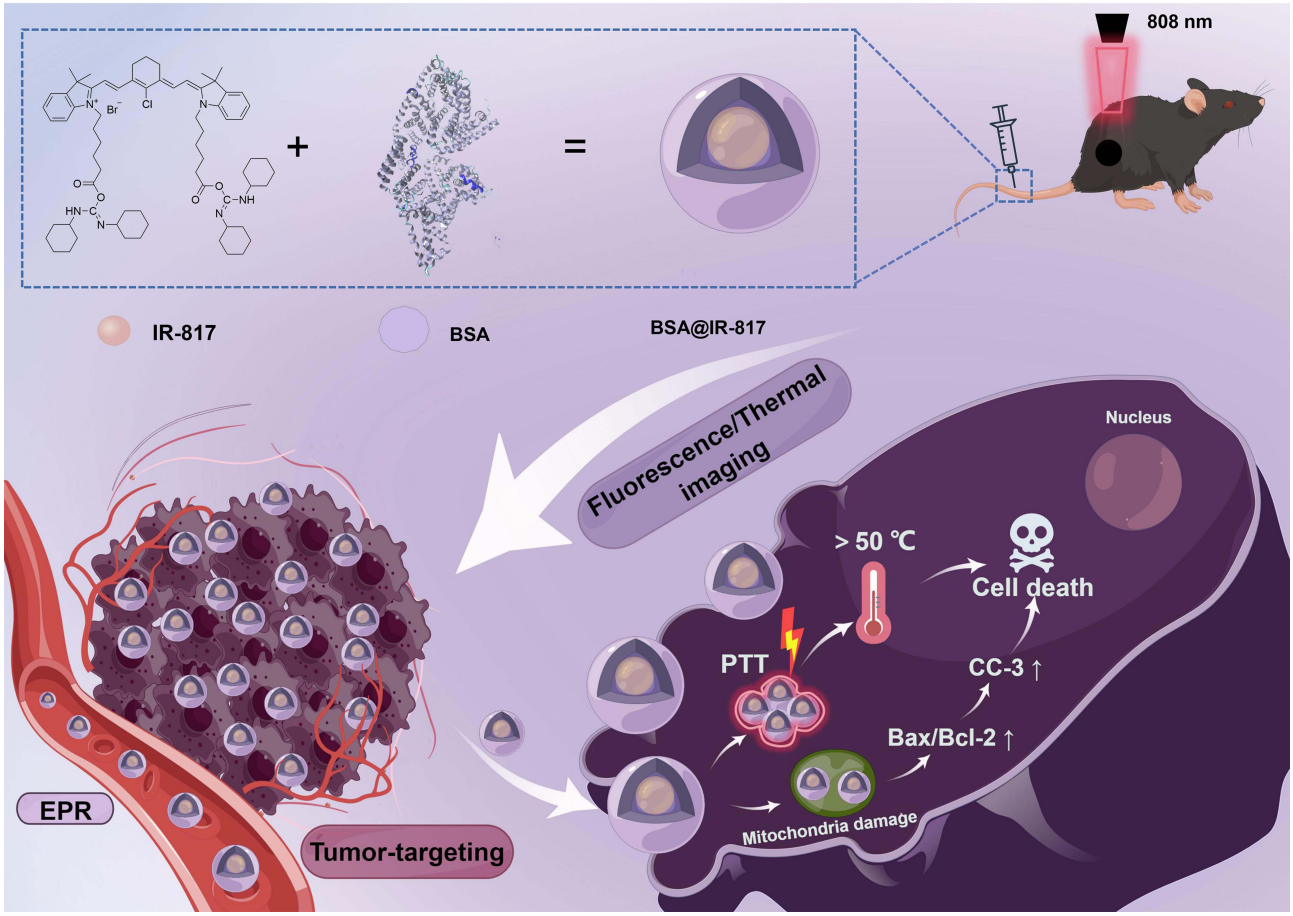

Scheme 1 Schematic illustration of BSA@IR-817 for NIR fluorescence image and photothermal therapy of melanoma. By Figdraw.

Powerful Antigen Retrieval Solution and Calcein/PI Live/Dead Assay kit and antibodies against Bcl-2 were purchased from Beyotime Institute of Biotechnology (Shanghai, China). Protein Loading Buffer, Multicolor Prestained Protein Ladder and 10% SDS-PAGE were from EpiZyme (Shanghai, China). Near-infrared dye IR-817 was synthesized following our previously reported protocol.[26] Antibodies against Ki-67 was purchased from Cell Signaling Technology (CST, Beverly, MA, USA). Antibodies against Cleaved caspase-3 (CC-3) was purchased from Zen-bio (Chengdu, China). Antibodies against Bax was purchased from Cell Signaling Technology (CST, Beverly, MA, USA).

Cell Culture

Human amelanotic melanoma lines A375 and mouse melanoma cell lines B16-F10 were obtained from ATCC (Manassas, V A, USA). All of the cells were cultured in Dulbecco's modified Eagle's medium containing 10% (v/v) fetal bovine serum and 1% (v/v) penicillin/streptomycin, with an atmosphere of 5% CO_2 at 37 °C.

Animal

Experimental animals were purchased in Southwest Medical University Animal Experimental Centre. All mice were C57BL/6J female mice age 6 to 8 weeks. They were kept in the animal house of Southwest Medical University, where the ambient temperature and humidity were kept within the normal range. The padding was changed every 2–3 days, allowing ad libitum eating and drinking. All animal procedures have been approved by the Laboratory Animal Management Committee of the Affiliated Hospital of Southwest Medical University in China (Permit Number: 20220812-022) and were conducted in accordance with the Chinese National Laboratory Animal-Guideline for Ethical Review of Animal Welfare.

Synthesis of Albumin@IR-817 Nanoparticles

HSA and BSA were respectively dissolved in PBS at a concentration of 10 μM and 160 μM, IR-817 was dissolved in DMSO at a concentration of 20 mM. Then BSA or HSA with IR-817 were mixed adequately according to the following manners. One way was the different concentrations (2.5, 5, 10, 20, 40, 80, 160 μM) with the same molar ratio (1:1), the other way was 10 μM IR-817 mixed with different concentrations of BSA or HSA to achieve different ratios (4:1, 3:1, 2:1, 1:1, 1:2, 1:3, 1:4). Finally, the mixture solution was placed in a 60 °C constant temperature water bath oscillator for 2 h heating and oscillation.

The optimal concentration and proportion of BSA@IR-817 solution (BSA: IR-817=30 μM: 10 μM) was selected for dialysis (MWCO of the dialysis bag was 3.5 KD) for more than 36 h, then the filtrate was dried with lyophilizer (Virtis Bench Top Lyophilizer, New York, USA) for 40 h. Finally, BSA@IR-817 lyophilized powder was redissolved in PBS and used to carry out subsequent experiments.

Characterization

The NIR absorption and emission spectra of HAS@IR-817, BSA@IR-817 were determined by a UV spectrophotometer (TU-1900, Puxi, Beijing, China) and FS5 spectrofluorometer (Edinburgh Instruments, Edinburgh, UK). The settings used were excitation 764 nm with 3 nm slit width and emission scan 780–900 nm with 2.5 nm slit width. The size distribution and zeta potential of BSA@IR-817 were determined using NanoBrook ZetaPlus Potential Analyzer (Brookhaven Instruments Corporation, New York, USA).

Scanning Electron Microscopy (SEM)

A small amount of BSA@IR-817 solution was dropped on the silicon wafer, and after drying, gold was sprayed for 30 s. The microstructure of BSA@IR-817 was observed by Hitachi SU8010 (Hitachi Limited Co, Hitachi, Japan) SEM, where the acceleration voltage was 3 kV and the test mode was secondary electron mode.

Gel Electrophoresis Analysis

First, the protein loading buffer was added to samples and thoroughly mixed. Then 10% sodium dodecylsulfate-polyacrylamide gels was prepared using Easy TM One-Step PAGE Gel Fast Preparation Kit. Finally, the appropriate samples were added to gel channel for electrophoresis (80 V for stacking gel and 120 V for separating gel). After electrophoresis, gels were analyzed in an Amersham Typhoon 5 Biomolecule imager (Cytiva) to detect the fluorescence signal of HSA@IR-817 and BSA@IR-817.

Calculating the Concentration of BSA@IR-817

A standard curve was established by detecting the corresponding absorption peaks of different concentrations of IR-817 in H_2O. Then 10 μL BSA@IR-817 solution was added into 2 mL H_2O to measure the absorption peaks and repeated three times. The concentration of IR-817 in BSA@IR-817 can be calculated according to the standard curve obtained above. When a new sample was prepared each time, a concentration determination was required. The standard BSA@IR-817 sample was 200 mL solution system each time, in which the concentration of IR-817 was 10 μM (2.352 mg). After being dialyzed and lyophilized, the mass of IR-817 in BSA@IR-817 was 1.986 mg according to the standard curve, so the encapsulation efficiency (EE) was 84.4%.

Hemolysis Test

Peripheral blood of the C57BL/6J mice venous plexus around the eyes was collected in anticoagulant tubes, and different concentrations of BSA@IR-817 were prepared in EP tubes. Meanwhile, PBS was used as negative control and H_2O was used as positive control. Then added 20 μL fresh peripheral blood, mixed in the EP tubes. After let stand for 24 h, the mixed solution was centrifuged at 2000 rpm for 5 min and taken photos. The supernatant was red after centrifugation, it indicated that hemolysis has occurred. Finally, the supernatant liquid was absorbed into the 96-well plate and the absorbance was measured using a Multiskan Sky spectrophotometer (Thermo Scientific, Waltham, MA, USA) Calculation formula of hemolysis rate: Hemolysis rate (%) = [OD (sample)-OD (PBS group)]/[OD (H_2O)-OD (PBS group)]×100%.

Intracellular Imaging

In order to detect the intracellular fluorescence imaging effect of BSA@IR-817, IR-817 and ICG, A375 and B16-F10 cells were inoculated into 6-well plates. Then, 10 μM BSA@IR-817, IR-817 and ICG were added and incubated for different time (0.5, 1, 2, 4, 8, 16 h), followed by Hoechst33342 (10 μg/mL) for 10 min. Finally, after washed with PBS for 3 times, the cells were performed on an inverted fluorescence microscope (Leica DMi8, Leica, Germany).

Tumor-Targeting NIR Fluorescence Imaging in vivo

B16-F10 cells were subcutaneously inoculated into the right hip of mice ($1x10^5$ cells per mouse). After the tumor grew to an appropriate size (about 800 mm^3), 100 μL 5 mg/kg BSA@IR-817, IR-817 or ICG was injected through the tail vein, respectively. After anesthetizing by pentobarbital sodium, all mice optical imaging were taken using the IVIS Lumina Series III Imaging System (PerkinElmer, Baltimore, MD, USA) at 0, 2, 6, 12, 24 h. The excitation/emission of BSA@IR-817, IR-817 was 620/710 nm and the excitation/emission of ICG was 760/810 nm. Fluorescence image analysis was conducted with the Living Image 4.5.2 software package.

Photothermal Properties in vitro

BSA@IR-817, BSA, IR-817 and ICG were added respectively into PBS and under 808 nm laser irradiation (Changchun New Industries [CNI] Model with PSU-H-LED) for 5 min according to different power density (0.5 W/cm^2, 0.8W/cm^2, 1W/cm^2) or different concentration (0, 5, 10, 20 μM). The temperature was recorded with FLUKE Ti32 thermal imager (Fluke Corporation, USA) every 30 s. In addition, the photothermal stability of BSA@IR-817, IR-817 and ICG were monitored under 4 periods of laser irradiation on/off (5 min each period).

In addition, the photothermal conversion efficiency (η) values were calculated according to the equation from the relevant report.[40,41] The temperature increase and decrease process was recorded by a thermal imager.

$$\eta = \frac{hs(T_{max} - T_{surr}) - Q_{dis}}{I\left(1 - 10^{-A_{808}}\right)}$$

$$hs = \frac{m_i C_{H_2O}}{\tau_s}$$

$$Q_{dis} = hs\left(T_{max,H_2O} - T_{surr}\right)$$

$$t = -\tau_s ln(\theta)$$

$$\theta = \frac{\mathrm{T} - T_{surr}}{T_{max} - T_{surr}}$$

where h is the thermal conductivity coefficient; s is the laser irradiation area; T_{max} is the maximum equilibrium temperature; T_{surr} is the surrounding ambient temperature; Q_{dis} is the thermal dissipation value of the solvent and container; I represents the laser power; and A_{808} represents the absorbance of dye at a wavelength of 808 nm. m_i represents the mass of deionized water; C_{H2O} is the heat capacity of deionized water (4.2 J/g)

Photothermal Properties in vivo

100 μL 4 mg/kg BSA@IR-817, IR-817 or ICG was intravenously injected into mice inoculated with B16-F10 cells (tumor volume was about 500 mm^3), using PBS as blank control. After injection 6 h, the mice were fixed, and the tumor site was exposed to laser 808 irradiation (1.0 W/cm^2) for 5 min, and the temperature was monitored and recorded every 30s with a thermal imager (Fluke Corporation, USA).

Cytotoxicity and Photocytotoxicity Evaluation of BSA@IR-817

In order to evaluate the toxicity and photothermal efficacy of BSA@IR-817, A375 and B16-F10 cells were inoculated into 96-well plates. After the cells were attached, the different concentration of BSA@IR-817 (0.31, 0.63, 1.25, 2.5, 5, 10, 20, 40, 80 μM) were added for 24 h; or using laser 808 to irradiate (1.0 W/cm^2) for 5 min after adding different concentration of BSA@IR-817 (0.16, 0.31, 0.63, 1.25, 2.5, 5, 10, 20 μM) to 6 h, and continue incubating for 24 h. At last, 20 μL MTT (5 mg/mL) was added for 2–4 h, then discarding the medium, 150 μL of DMSO was added into each well. The absorbance was measured at 490 nm by a microplate tester (Spectra MAX 340, Molecular Devices, USA).

Calcein AM/PI Staining

Calcein AM combined with Propidium Iodide (PI) can be used for the detection of cell activity and cytotoxicity by double fluorescence staining of living and dead cells simultaneously. Firstly, the cells were inoculated into 96-well plates, after the cells were attached to the wall, 20 μM BSA@IR-817 was added for 6 h (using PBS as blank control). After that, the cells were irradiated with laser 808 for 5 min (1.0 W/cm^2) and incubated for 24 h. The cells were stained for 30 min using the Calcein AM/PI Cell Viability/Cytotoxicity Assay Kit according to the manufacturer's instructions, washed with PBS and photographed under an inverted fluorescence microscope (Leica DMi8, Leica, Germany).

Photothermal Therapy in vivo

The melanoma mouse model was constructed by subcutaneously inoculating B16-F10 cells (4×10^8 cells/mouse) into the right hip of mice. When the tumor grew to about 50 mm^3, the mice were randomly divided into 6 groups: Control group (just injected with PBS), Laser group (laser irradiation after injected with PBS), and IR-817 group, BSA@IR-817 group, IR-817+Laser group, BSA@IR-817+Laser group, 8–9 mice in each group. Administration mode: caudal vein injection and the doses of IR-817 and BSA@IR-817 were 4 mg/kg, 100 μL/mouse; Frequency: once every other day. The group requiring laser irradiation was 6 h after caudal vein administration, and the irradiation power was 1.0 W /cm^2 for 5 min. Body weight and tumor volume were measured every 2 days. Tumor volume (mm^3) = 0.5 × long diameter × short diameter^2. After 10 days, parts of mice were sacrificed by cervical dislocation, organs and tumors were dissected to fix in 4% formaldehyde solution. Survival status of the remaining mice was recorded, and death was determined when the tumor volume was larger than 2000 mm^3.

Histological Examination

After tumors and organs of mice fixed with formaldehyde underwent a series of dehydrated steps, the tissues were embedded in paraffin wax and sliced at a thickness of 4 μm using a Leica RM2125 slicer. Then the sections were stained with hematoxylin eosin and sealed with neutral resin. Finally, images were collected on an Olympus BX43 Upright Microscope.

Immunohistochemical Examination

Immunohistochemistry was carried out by conventional methods.[42] In short, after a series of dehydrating and embedding of tissues, 4 μm tissue slices were obtained and were roasted for 2 h at 65 °C, dewaxed with xylene, and repaired with citric acid buffer (pH 6.0). After the general SP kit was used according to the manufacturer's instructions and using primary antibody (Ki-67, CC-3, Bax, Bcl-2), Diaminobenzidine (DAB) color developing agent was added, hematoxylin was re-dyed for 2 min, and resin was used to seal the slides. Finally, images were collected on an Olympus BX43 Upright Microscope.

Statistical Analysis

All experiments were repeated at least 3 times, data analyses were performed using GraphPad Prism 9.0 software and the data were presented as mean ± SD. Asterisks indicate significant differences (*$p < 0.05$, **$p < 0.01$, ***$p < 0.001$, ****$p < 0.0001$) by unpaired Student's two-sided t-test.

Results

Rational Screening Process of HSA@IR-817 and BSA@IR-817

Due to the presence of both hydrophilic and hydrophobic domains in albumin, hydrophobic compounds such as cyanine dyes can induce the self-assembly of albumin molecules through their hydrophobicity.[43] Other than that, some relevant studies have also confirmed that chlorine-containing cyanine dyes can form covalent bonds with albumin.[44,45] Correspondingly, we hypothesized that the novel cyanine dye IR-817, which was synthesized by our groups, could also bound with albumin and undergo some property changes. Therefore, the two functional proteins HSA and BSA were selected to investigate their role in the modification of IR-817's properties. In order to determine the optimal concentration and ratio of HSA or BSA combined with IR-817, HSA@IR-817 and BSA@IR-817 were prepared with different concentrations (2.5, 5, 10, 20, 40, 80, 160 μM) and a molar ratio of albumin/IR-817 of 1:1, based on the findings of Shoujun Zhu et al.[46,47] Additionally, their respective fluorescence emission spectra were detected. As depicted in Figure 1A and B, when the concentration was 10 μM, the fluorescence of HSA@IR-817 and BSA@IR-817 was the strongest, and the fluorescence of BSA@IR-817 was stronger than HSA@IR-817. Concurrently, we discovered that the fluorescence intensity of HSA@IR-817 and BSA@IR-817 decreased rapidly with increasing concentration and that mainly due to the inability of an excessive amount of dye to bind with albumin caused the ACQ effect, which was consistent with previous research.[47] Therefore, we selected 10 μM IR-817 to investigate the optimal ratio of albumin binding. As shown in Figure 1C and D, when the ratio of BSA to IR-817 was ≥1, the fluorescence was significantly enhanced, and the ratio of 3:1 produced the strongest fluorescence. Similarly, HSA@IR-817 exhibited the strongest fluorescence when the ratio of HSA to IR-817 was 2:1. This could be explained that when the concentration of IR-817 all was 10 μM, with the higher concentration of albumin, an albumin could bind to the less IR-817. However, the combining ability of one albumin molecule was limited, when the albumin concentration was too low, the more free dye IR-817 could make the fluorescence intensity more lower. Subsequently, we used gel electrophoresis to explore the binding of albumin to IR-817. As depicted in Figure 1E and F, the range of albumin molecular weight (50–70 kDa) displayed distinct fluorescence bands, and the trend was essentially consistent with the fluorescence emission. After preparing BSA@IR-817 and HSA@IR-817 at various concentrations above running gel electrophoresis, it was discovered that the

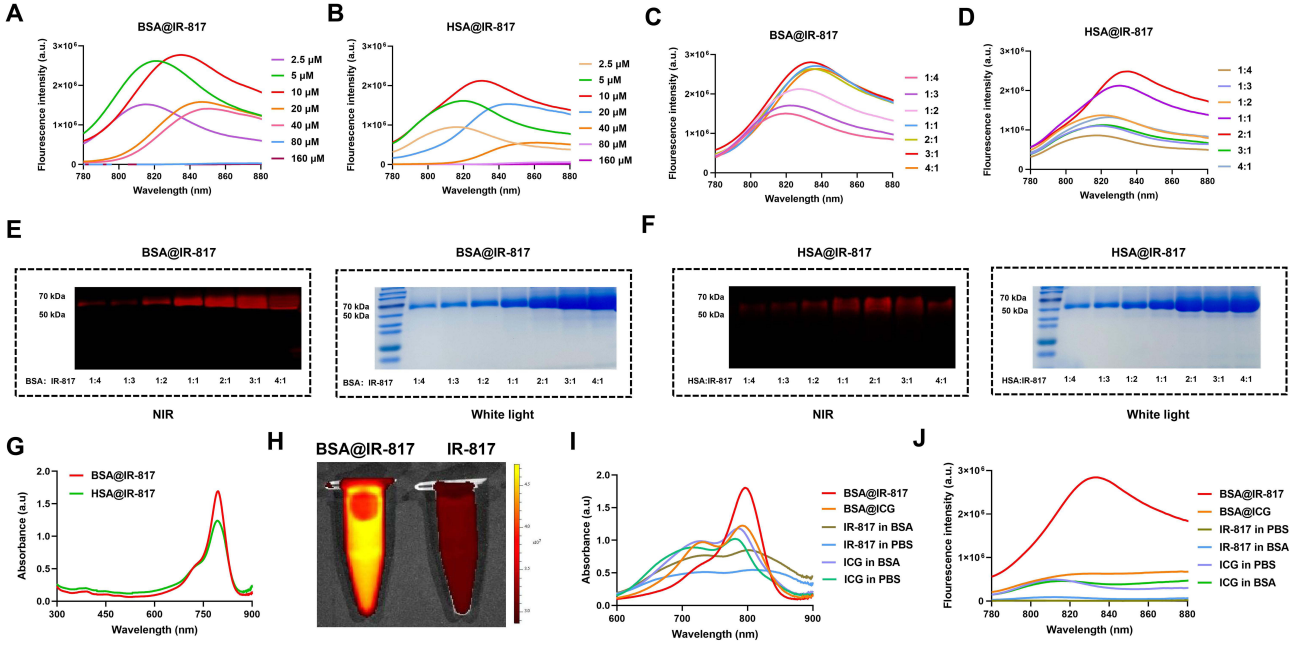

Figure 1 Rational screening process of HSA@IR-817 and BSA@IR-817. Fluorescence emission spectra of different concentrations of (**A**) BSA@IR-817 and (**B**) HSA@IR-817 with the molar ratio of albumin/IR-817 as 1:1 in PBS. Fluorescence emission spectra of 10 μM IR-817 mixed with different concentrations of (**C**) BSA or (**D**) HSA to achieve different ratios (4:1, 3:1, 2:1, 1:1, 1:2, 1:3, and 1:4). Electrophoresis gel analysis of (**E**) BSA@IR-817 and (**F**) HSA@IR-817 in NIR and white light. (**G**) Infrared absorption spectra of BSA@IR-817 and HSA@IR-817 (10 μM, 1:1). (**H**) NIR image of 10 μM BSA@IR-817 and IR-817 in an EP tube. (**I**) Infrared absorption spectra and (**J**) fluorescence emission spectra of 10 μM BSA@IR-817, BSA@ICG, IR-817 in BSA, IR-817 in PBS, ICG in BSA, and ICG in PBS.

fluorescence intensity of BSA@IR-817 and HSA@IR-817 varied as a function of concentration (Figure S1A–D). Correspondingly, we hypothesized that the separation of free and unbound dyes by gel electrophoresis made a decrease in the ACQ effect of IR-817 could be the reason of fluorescence enhancement. Moreover, the measurement of absorption wavelength not only confirmed that BSA@IR-817 and HSA@IR-817 had strong absorption peaks at 764 nm but also demonstrated that the combination effect of IR-817 with BSA was superior to that of HSA (Figure 1G). Therefore, BSA@IR-817 was finally selected for the subsequent experiments.

Near-infrared images of BSA@IR-817 and IR-817 were captured using the IVIS imaging system. Due to its poor water solubility, IR-817 exhibited weak fluorescence in PBS, as depicted in Figure 1H. However, this defect could be significantly mitigated by combining BSA with IR-817 to form BSA@IR-817 nanoparticles, which increased the fluorescence intensity and were confirmed by the detection of the absorption and emission peak (Figure 1I and J). Correspondingly, we discovered that IR-817 mixed with BSA alone was incapable of producing the same result. In addition, we prepared BSA@ICG nanoparticles using the same ICG concentration and method as the control. Absorption and fluorescence emission measurements revealed that BSA@IR-817 was considerably more potent than ICG and BSA@ICG (Figure 1I and J).

Characterization of BSA@IR-817 Nanoparticles

The BSA@IR-817 (30 μM: 10 μM) solution with the optimal proportion and concentration was used for dialysis and lyophilization, yielding BSA@IR-817 for further experimental study. Absorption spectroscopy was used to determine the absorption peaks corresponding to the various concentrations of IR-817 in H_2O, and standard curves were drawn (Figure S2A and B). Subsequently, the concentration of BSA@IR-817 was calculated according to the standard curves. The morphology and size of BSA and BSA@IR-817 nanoparticles were characterized using scanning electron microscopy (SEM) and dynamic light scattering (DLS). As depicted in Figure 2A and B, the combination of BSA and IR-817 could form uniformly dispersed nanoparticles with an average particle size of 176.4 nm; the polydispersity index (PDI) of BSA@IR-817 was determined to be 0.147. This nanoparticle size can induce an enhanced permeability and retention (EPR) effect in tumor tissues, which

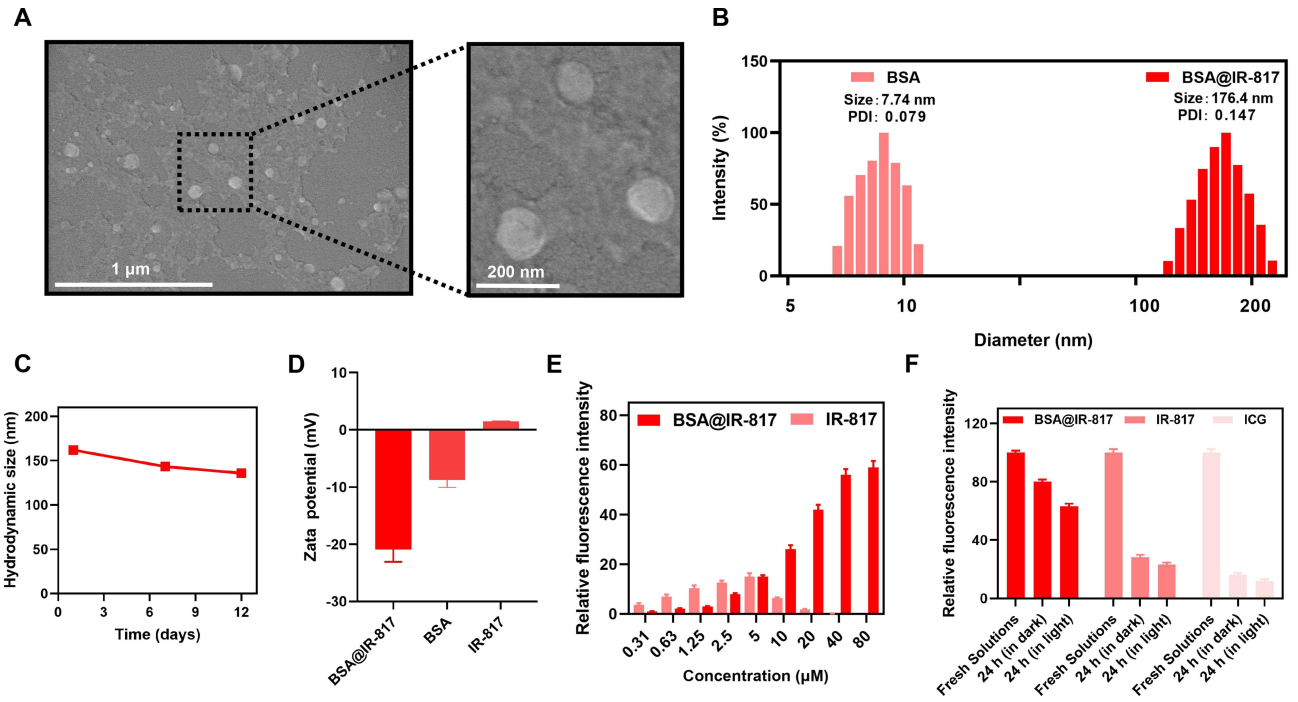

Figure 2 Characterization of BSA@IR-817 nanoparticles. (**A**) Scanning electron microscopy (SEM) image of BSA@IR-817. Scale bars: 1 μm (left image); 200 nm (right image). (**B**) Hydrodynamic size distribution of BSA and BSA@IR-817. (**C**) The hydrodynamic diameter of BSA@IR-817 during 12 days. (**D**) Zeta potential of BSA@IR-817, BSA, and IR-817. (**E**) The relative fluorescence intensity of BSA@IR-817 and IR-817 at different concentrations. (**F**) The relative fluorescence intensity of 10 μM BSA@IR-817, IR-817, and ICG right after the dilution process or 24 h of storage (in light or dark).

promotes nanoparticle retention in tumor tissues.[48] In addition, the stability of BSA@IR-817 was evaluated by observing the hydrodynamic size of the protein for approximately 12 days in water, which showed minimal variation in size (Figure 2C). Zeta potential measures the force of mutual repulsion or attraction between particles; if the absolute value (positive or negative) is greater, the system is more stable.[49] Compared to BSA (−8.77 ± 1.28 mV) and IR-817 (1.485 ± 0.05 mV), the absolute value of BSA@IR-817's zeta potential (−20.95 ± 2.15 mV) was the highest (Figure 2D).

One of the unavoidable disadvantages of cyanine dyes is the ACQ effect, which has been observed in numerous cyanine dyes.[50] Therefore, for the detection of the fluorescence emission spectrum, various concentrations of BSA@IR-817 or IR-817 were dissolved in H_2O. The fluorescence intensity corresponding to the highest peak value of 0.31 μM BSA@IR-817 was set to "1", and the fluorescence intensity of other concentrations was its relative ratio. As depicted in Figure 2E, when the concentration of IR-817 exceeded 5 μM, the fluorescence significantly decreased due to the ACQ effect. However, the fluorescence intensity of BSA@IR-817 did not decrease as the concentration increased, indicating that BSA as a carrier could effectively mitigate the fluorescence ACQ effect of IR-817. We compared the photostability of BSA@IR-817 to that of IR-817 and ICG. The absorption and emission spectra immediately after dilution or 24 h of storage (in light or darkness) revealed that the fluorescence and absorption of IR-817 and ICG decreased significantly after 24 h of storage, whereas BSA@IR-817 remained relatively stable (Figures 2F and S3). In conclusion, these observations indicated that IR-817 was stably incorporated into BSA to form stable BSA@IR-817 nanoparticles that are amenable to further investigation.

The Fluorescence Imaging of BSA@IR-817 in vitro and in vivo

A375 and B16-F10 cells were incubated with BSA@IR-817, IR-817 and ICG for 0.5, 1, 2, 4, 8, 16 h, respectively. Fluorescence images were captured as depicted in Figure 3A and B, and Figure S4, BSA@IR-817 began emitting

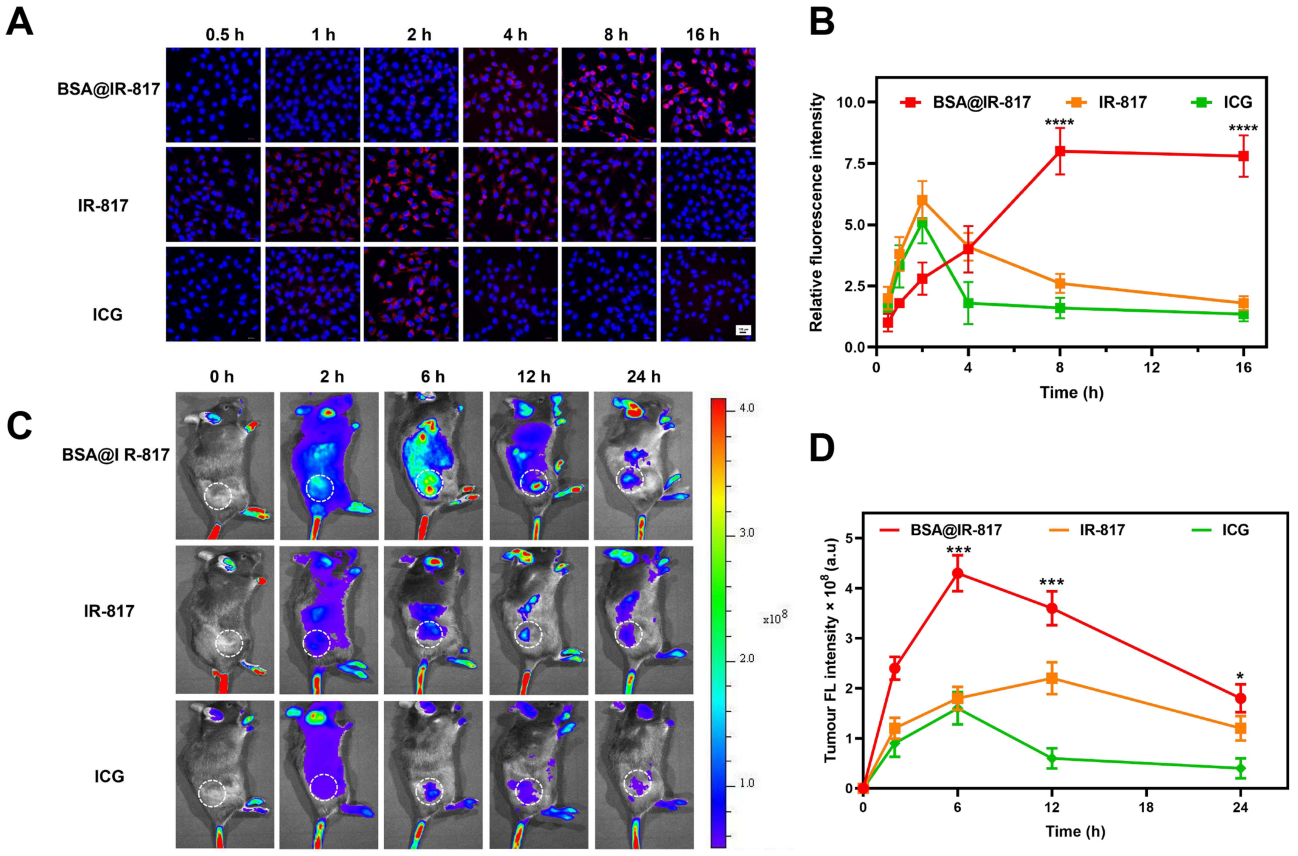

Figure 3 The fluorescence imaging of BSA@IR-817 in vitro and in vivo. (**A**) The fluorescence images of B16-F10 cells were incubated with 10 μM BSA@IR-817, IR-817, and ICG for different times (0.5, 1, 2, 4, 8, and 16 h). (**B**) The quantification of relative fluorescence signal intensity in (**A**) changed over time. (**C**) Fluorescence imaging of the mice at different time points (0, 2, 6, 12, and 24 h) after intravenous injection of BSA@IR-817, IR-817, and ICG. The white dashed circle indicated the inoculated tumor area in the mice. (**D**) Fluorescence statistics of BSA@IR-817, IR-817, and ICG in mice. Values represent the mean ± SD, * p <0.05, *** p <0.001, **** p <0.0001, compared with the other two groups.

fluorescence ~4 h after entering the cells, and the fluorescence was strongest at 8 h, being stronger than IR-817 and ICG. Although IR-817 and ICG were able to rapidly enter cells, their fluorescence decreased significantly after 4 h and 2 h, respectively, whereas BSA@IR-817 showed no significant change after 16 h. It was discovered that BSA@IR-817 enhanced the fluorescence intensity and stability of IR-817 at the cellular level.

In addition, the tumor-targeting imaging capabilities of BSA@IR-817, IR-817, and ICG were evaluated in mice. Accordingly, BSA@IR-817, IR-817, and ICG (5 mg/kg) were injected via the caudal vein into B16-F10 cell-inoculated C57BL/6J mice. Fluorescence changes at tumor sites were observed by capturing images at various time intervals using an imaging system for small animals. As depicted in Figure 3C, BSA@IR-817 reached its maximum accumulation of fluorescence at the tumor site at 6 h, after which the non-specific accumulation at other sites would be gradually metabolized, but the fluorescence at the tumor site would remain visible for 24 h. In contrast, IR-817 and ICG displayed less accumulation in tumors, weaker fluorescence, and shorter tumor retention times. In Figure 3D, the relative intensity of the fluorescence signal at the tumor site was plotted against time, further demonstrating the excellent imaging effect and tumor-targeting ability of BSA@IR-817 in vivo.

Evaluations BSA@IR-817 Photothermal Properties

To determine the photothermal properties of BSA@IR-817, various power densities of laser 808 (0.5, 0.8, and 1 W/cm^2) were employed. As showed in Figure 4A, as the irradiation power increased, the temperature increase (ΔT) of BSA@IR-817 at 20 μM also increased (from 11.5 °C to 27.6 °C). Additionally, it was demonstrated that the photothermal heating capacity of BSA@IR-817 was dependent on laser power. Then, the effect of BSA@IR-817 concentration was evaluated at 1 W/cm^2, and the results showed that ΔT decreased when BSA@IR-817 concentration decreased (Figure 4B). To further characterize BSA@IR-817, IR-817, ICG, and BSA, we compared their photothermal efficacy. Accordingly, the temperature increase of BSA@IR-817 (ΔT = 27.6 °C) was greater than that of IR-817 (ΔT = 15.7 °C), ICG (ΔT = 14.1 °C), and BSA (ΔT = 6.6 °C) (1 W/cm^2, 5 min) (Figure 4C and D). Additionally, the photothermal stability of BSA@IR-817 was determined. In four heating and cooling cycles, it was observed that BSA@IR-817, IR-817, and ICG exhibited varying degrees of temperature decreases in the second cycle, and then remained relatively stable The ΔT of BSA@IR-817 was, however, consistently greater than that of IR-817 and ICG (Figure 4E). In order to make a more straightforward comparison between BSA@IR-817, IR-817 and ICG in photothermal capabilities, we calculated their photothermal conversion efficiency (PCE) values as 32.6%, 12.6% and 9.2%, respectively, according to the initial heating-cooling cycle temperature changes (Figure 4F). The aforementioned results, therefore, confirmed that BSA@IR-817 exhibited a more superior photothermal property than the other two groups, which bodes well for its future use. Finally, the photothermal changes of BSA@IR-817 were investigated in vivo in subcutaneous tumor-bearing mice with B16-F10 cells. After 6 h of injection of 5 mg/kg BSA@IR-817, IR-817, or ICG through the caudal vein, mice were irradiated with laser 808 (1 W/cm^2) for 5 min, and changes in temperature were recorded every 30 s. The infrared thermal imaging of mice after different irradiation times was depicted in Figure 4G. As observed, the increase in temperature at the tumor site of mice in the BSA@IR-817 group was significantly greater than that of IR-817 and ICG. According to the curve of specific temperature versus irradiation time, the maximum temperature of BSA@IR-817 in vivo could reach 52.3 °C, which was lethal to tumor cells, whereas IR-817 and ICG could only reach 42.1 °C and 39.5 °C, respectively (Figure 4H). In conclusion, BSA@IR-817 exhibited a favorable photothermal effect in vitro and in vivo and may be an ideal photothermal treatment reagent.

Photoinduced Cytotoxicity of BSA@IR-817 in Melanoma Cells

In order to detect the photoinduced cytotoxicity of BSA@IR-817, A375 and B16-F10 cells were incubated with different concentrations of BSA@IR-817 for 24 h, after which MTT reagent was used to detect cell viability for evaluating the cytotoxicity of BSA@IR-817. As shown in Figure 5A, even at a high concentration (80 μM), the cell viability was ~60%, whereas previous studies confirmed that the cell viability of A375 and B16-F10 after 24 h of treatment with 10 μM IR-817 was ~10%.[26] This indicated that BSA@IR-817 could reduce the toxicity of IR-817 significantly. Subsequently, BSA@IR-817 was validated as a photothermal agent for the laser-induced ablation of cancer cells. When the cells were incubated with 20 μM BSA@IR-817 for 6 h and then exposed to laser irradiation (1 W/cm^2) for 5 min, cell viability was reduced by 80–90% after 24 h (Figure 5B). Moreover, in the live/dead staining experiments, the ability of BSA@IR-817 to kill cancer cells was also observed through the co-staining of Calcine AM and propidium iodide (PI) cells. As anticipated, laser irradiation of BSA@IR-817 resulted in nearly

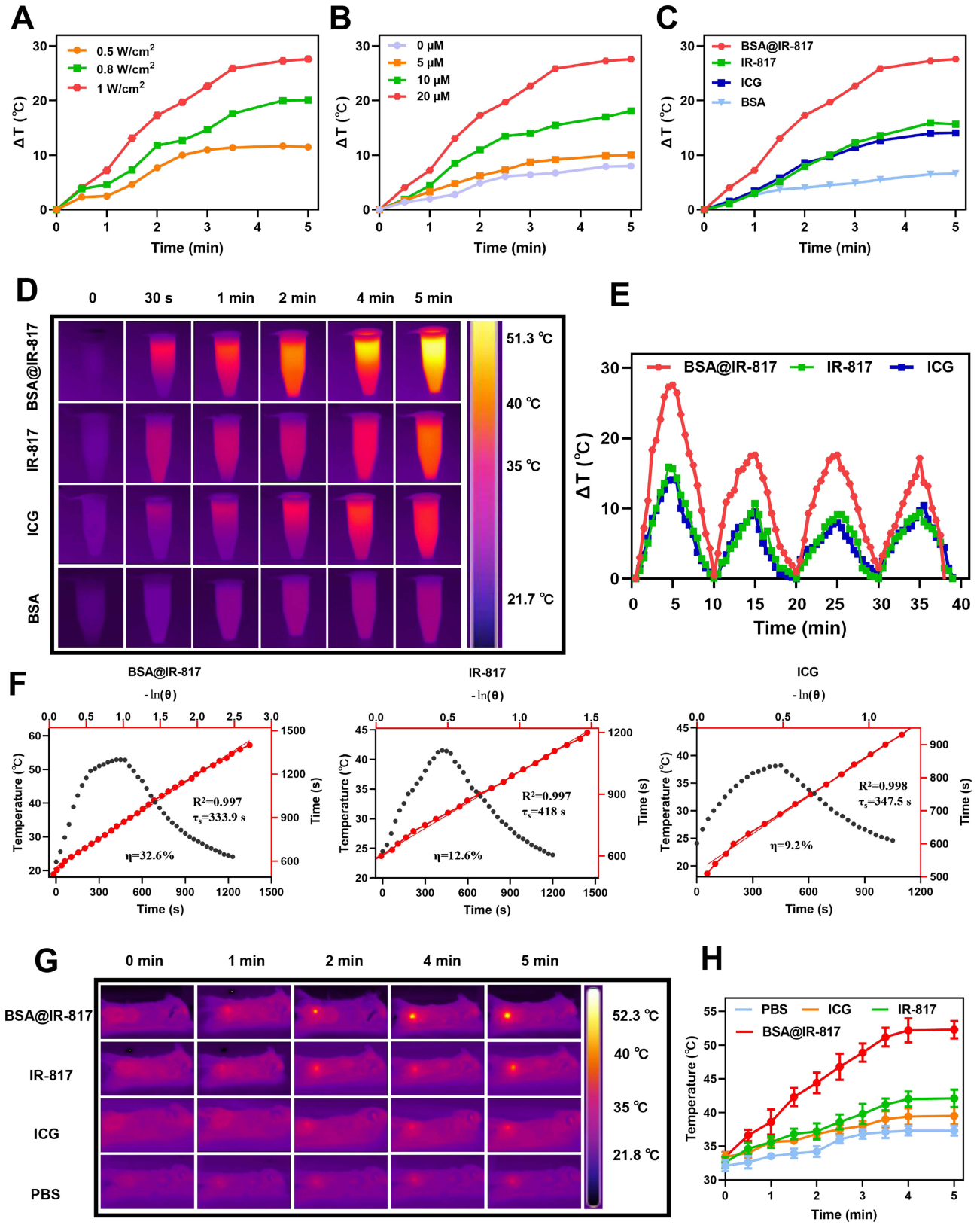

Figure 4 Evaluations BSA@IR-817 photothermal properties. (**A**) Temperature increase of BSA@IR-817 (20 μM) in PBS under an 808 nm laser with different exposure intensities (0.5, 0.8, 1 W/cm^2). (**B**) Temperature increase of BSA@IR-817 at different concentrations (0, 5, 10, and 20 μM) under an 808 nm laser (1 W/cm^2). (**C**) Temperature change of BSA@IR-817, IR-817, ICG and BSA (20 μM) upon exposure to 808 nm laser (1 W/cm^2) for different intervals. (**D**) Infrared thermal images of (**C**). (**E**) Temperature changes of BSA@IR-817, IR-817 and ICG during four circles of heating-cooling processes (1 W/cm^2, 5 min). (**F**) Photothermal conversion efficiency (PCE) of BSA@IR-817, IR-817 and ICG (20 μM, 1 W/cm^2). (**G**) Infrared thermographic images of the B16-F10 cell tumor-bearing mice after irradiation (1 W/cm^2, 5 min). (**H**) Change in tumor temperature as a function of the irradiation time.

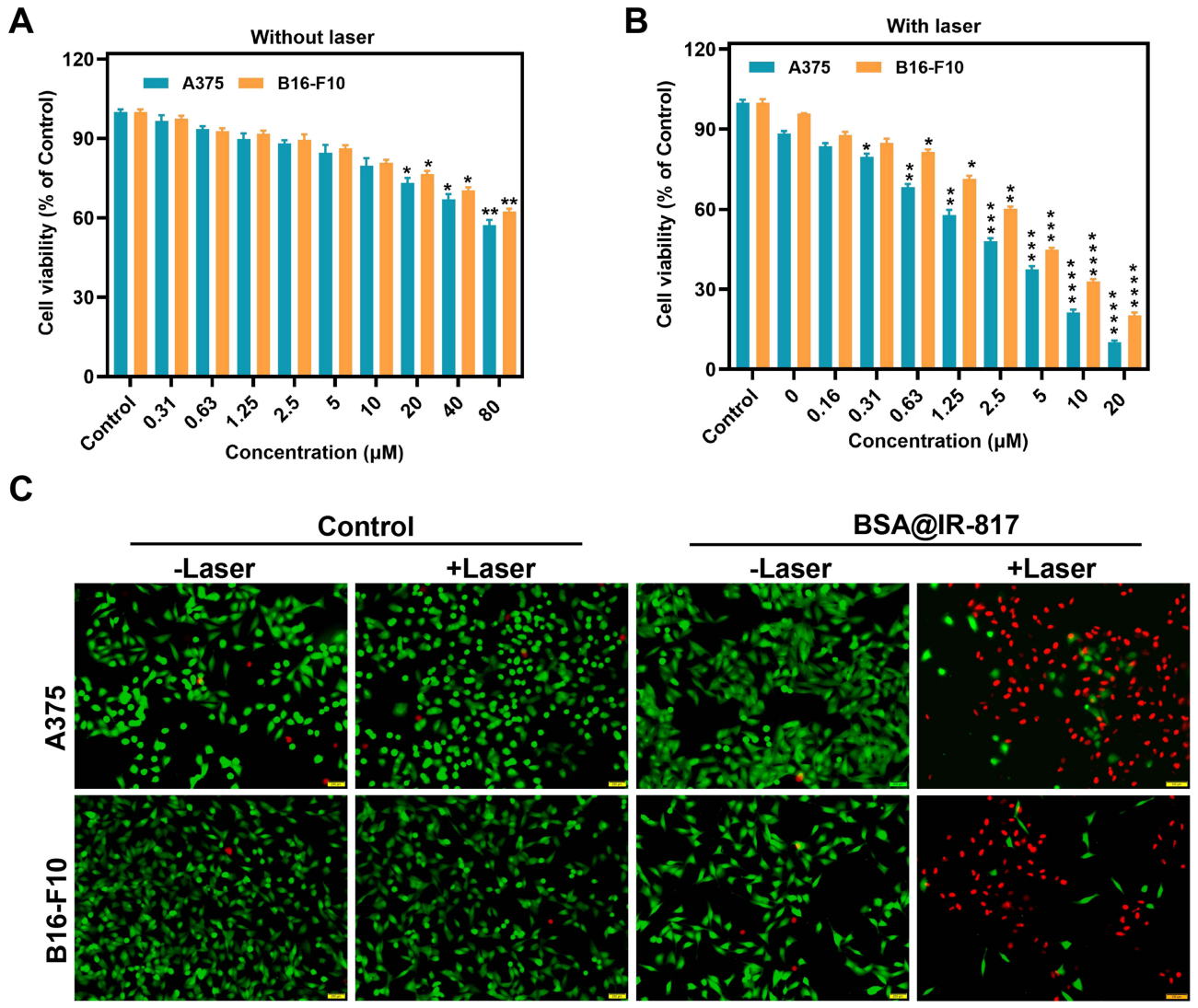

Figure 5 Photoinduced cytotoxicity of BSA@IR-817 in melanoma cells. (**A**) Viabilities of cancer cells incubated with BSA@IR-817 for 24 h. (**B**) Photoinduced toxicity of cancer cells treated with BSA@IR-817 of different concentrations following 808 nm laser irradiation (1 W/cm^2) for 5 min and continued incubation for 24 h. (**C**) Fluorescence images of Calcein AM/PI co-stained A375 and B16-F10 cells with BSA@IR-817 (10 μM) incubation after being exposed to the 808 nm laser (1 W/cm^2, 5 min). Values represent the mean ± SD, * p <0.05, ** p <0.01, *** p <0.001, **** p <0.0001, compared with the control group.

complete cell death (red emission in Figure 5C). In contrast, almost no phototoxicity was observed in cells treated with an 808 nm laser alone, indicating that the laser power densities (1 W/cm^2) have minimal side effects. Thus, the aforementioned results indicate that BSA@IR-817 has great photothermal treatment potential.

Photo-Therapeutic Efficacy Evaluation of BSA@IR-817 in vivo

In light of the aforementioned findings, we evaluated the in vivo effects of photothermal therapy. The melanoma mouse model was constructed by subcutaneously inoculating B16-F10 cells (4×10^8 cells per mouse) into the right hip of mice. When the tumor grew to 50 mm^3, the mice were treated with PBS, IR-817, or BSA@IR-817. The drug was administered through the caudal vein once every other day for a total of three treatments; the detailed experimental protocol is depicted in Figure 6A. The tumor entity map, tumor growth curve, and tumor weight statistics were depicted graphically in Figure 6B-D, and the tumor growth of each mouse was recorded simultaneously (Figure 6E). The results demonstrated that BSA@IR-817 only marginally inhibited tumor growth, whereas the photothermal treatment of BSA@IR-817 after laser 808 irradiation was able to effectively inhibit tumor growth, with an inhibition rate of over 99%. Concurrently, we discovered that mice injected with the same concentration of IR-817 exhibited obvious toxic side effects, resulting in a rapid loss of body weight and that they all perished approximately 7 days after administration. Nevertheless, there was no significant difference in body weight between mice injected with BSA@IR-817 and

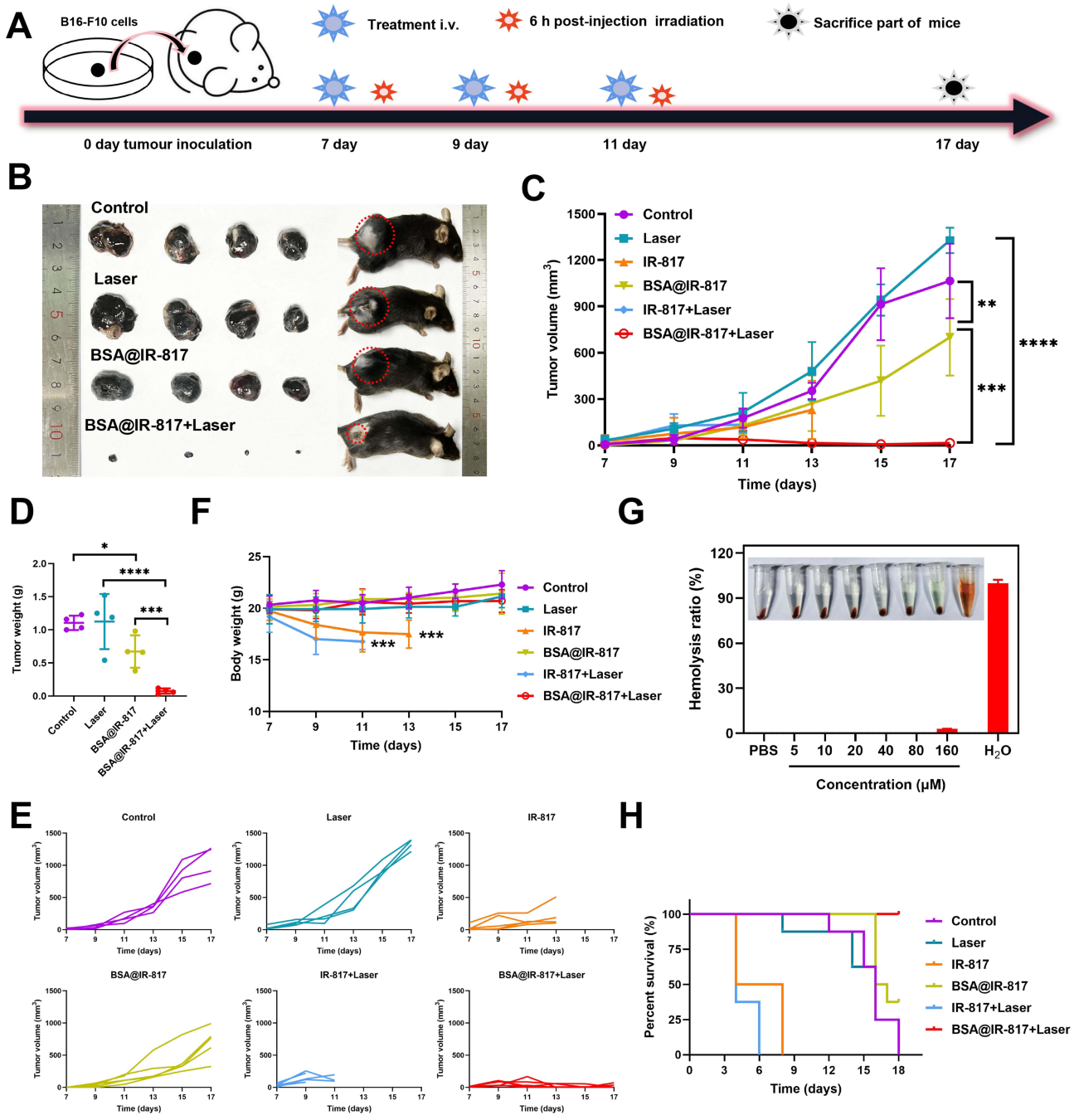

Figure 6 Photo-therapeutic efficacy evaluation of BSA@IR-817 in vivo. (**A**) Establishment of B16-F10 tumor-bearing mice model, administration, and laser irradiation to the mice. (**B**) Photos of mice bearing B16-F10 tumor and anatomic tumor on day 10 after various treatments as indicated. (**C**) The tumor growth in B16-F10 tumor-bearing mice treated by different formulations. (**D**) Tumor weight. (**E**) The tumor growth curves of each group. (**F**) Body weight changes of mice. (**G**) Blood safety evaluation of different concentrations of BSA@IR-817. (**H**) The survival curves of the tumor-bearing mice. Values represent the mean ± SD, *p <0.05, **p <0.01, ***p <0.001, ****p <0.0001.

the control group (Figure 6F). It suggested that BSA@IR-817 possessed a high level of biological safety, which was confirmed by the hemolysis experiment (Figure 6G). According to the survival curve of mice after 18 days, mice in the BSA@IR-817+Laser group were still alive, whereas mice in the other groups were gradually dying (Figure 6H). In conclusion, BSA@IR-817 exhibited significant phototherapeutic efficacy in inhibiting tumor growth.

Histological Analysis

To further assess the effects of BSA@IR-817 and IR-817 on the organs of mice, the heart, liver, spleen, lung, and kidney were stained with hematoxylin and eosin (H&E) (Figure 7A). The liver and kidney of IR-817 and IR-817+Laser-treated

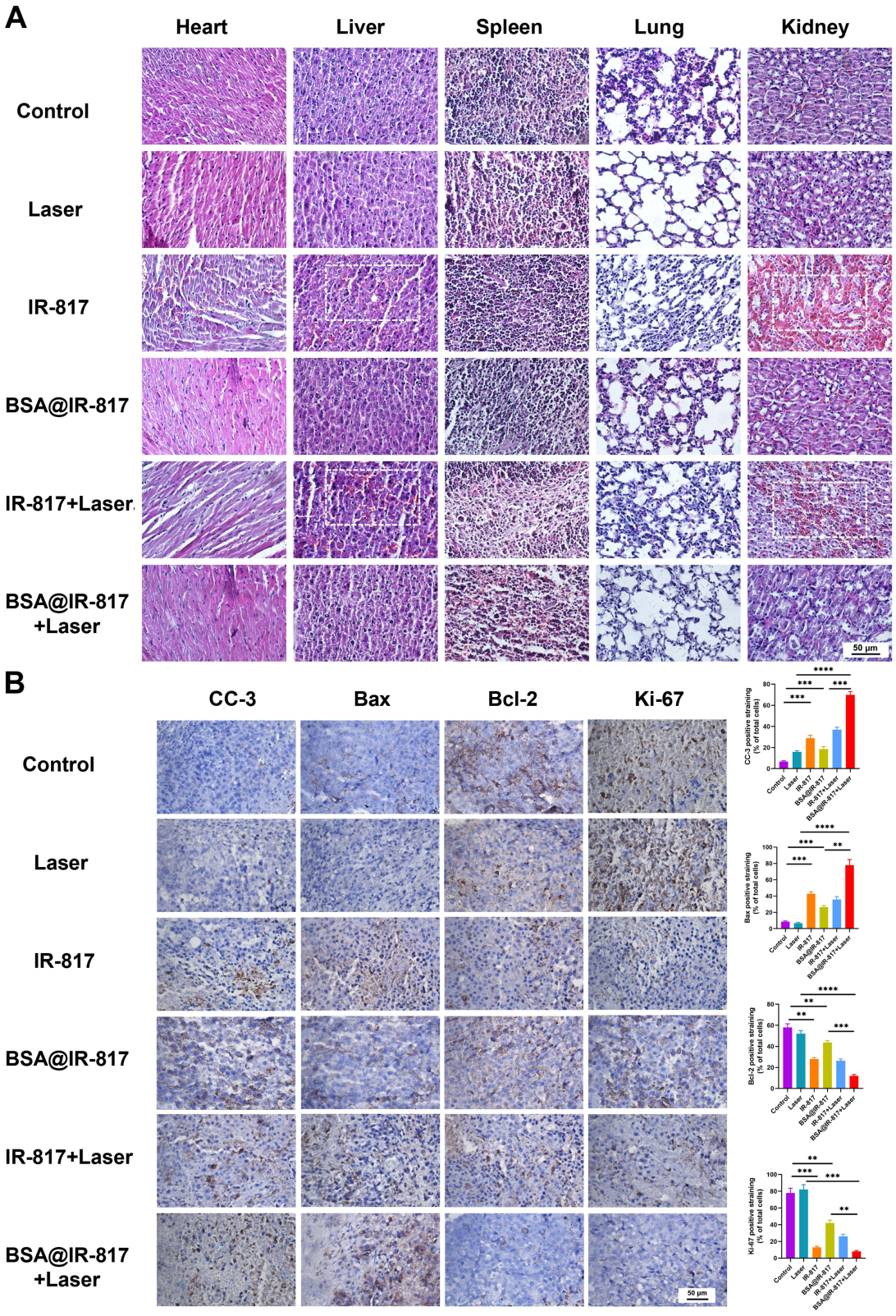

Figure 7 Histological analysis. (**A**) Representative histological features of the major organs of the tumor-bearing mice with various treatments. Scale bars, 50 μm (**B**) Ki-67, CC-3, Bax, and Bcl-2 immunohistochemical staining of tumor sections in the mice. Scale bars, 50 μm. Values represent the mean ± SD, n = 3. ***p* <0.01, ****p* <0.001, *****p* <0.0001.

mice exhibited significant hemorrhaging and necrosis (highlighted by the white line in the Figure), which may be the primary cause of rapid death in mice. BSA@IR-817 was identical to the control group; there were almost no lesions in the organs, demonstrating once again that BSA@IR-817 significantly reduced the toxic and side effects of IR-817 and had high biological safety, which was anticipated to be studied further and applied in vivo. Our previous studies showed that IR-817 could induce mitochondrial swelling, vacuolation, and a decrease in mitochondrial count (Figure S5). Additionally, it was confirmed that IR-817 promoted Bax and inhibited Bcl-2 protein expression, thus initiating a caspase cascade.[26] We believed that this was also one of the reasons why BSA@IR-817, without laser irradiation, could exert some antitumor effects. Consequently, the expressions of CC-3, Bax, Bcl-2, and Ki-67 (the tumor proliferation marker) were detected by immunohistochemistry in the tumors of mice from each group (Figure 7B). As anticipated, positive expressions of CC-3 and Bax were increased in the non-laser BSA@IR-817 group compared to the control group, while expression of Bcl-2 was suppressed. This trend was also increased in the BSA@IR-817+Laser group. Therefore, the result indicated that BSA@IR-817 might indeed induce cell apoptosis via the mitochondrial apoptosis pathway. In addition, Ki-67 staining revealed that laser irradiation significantly inhibited tumor proliferation in BSA@IR-817 cells.

Discussion

In previous research, we successfully synthesized IR-817, a novel mitochondria-targeted NIR fluorescent probe, and investigated its mechanism of action in melanoma. As a cyanine dye derivative, IR-817 has demonstrated excellent diagnostic and therapeutic imaging effects in melanoma. Despite this, IR-817 is still plagued by issues such as poor water solubility, the ACQ effect, photobleaching, a short imaging time, and toxic side effects. According to relevant studies, certain hydrophobic regions of albumin can combine with certain cyanine dyes to form the albumin@dye complex, which improves the biocompatibility and photostability of the dyes. In addition, albumin encapsulation will produce nanoparticles with a relatively large size and a long half-life in the blood, which will increase the circulating time of dyes within the body.[46] In light of the aforementioned, we sought a suitable albumin to enhance IR-817's diagnostic and therapeutic efficacy and reduce its toxicity.

Through a rational screening process, we found that the fluorescence decreased sharply when the ratio of albumin to IR-817 was less than 1. This was primarily due to the ACQ effect, which was caused by the excess of unbound dye. While the ratio of BSA to IR-817 was 3:1 and the concentration of IR-817 was 10 μM, the fluorescence of BSA@IR-817 was the strongest, and its peak fluorescence and absorption values were greater than those of HSA@IR-817. Albumin has been immobilized with ICG for NIR fluorescence imaging and phototherapy under single-wavelength excitation.[51] To compare BSA@IR-817 with BSA@ICG, we prepared BSA@ICG in the same manner and discovered that the fluorescence and absorption of BSA@IR-817 were significantly greater than those of BSA@ICG. A possible explanation for this might be the relatively low hydrophobicity of ICG, which resulted in unstable binding affinity.[52] However, the structure of IR-817 contains chlorine, which binds to BSA to produce a more stable and brilliant albumin@dye nanoparticle probe.[47] BSA@IR-817 nanoparticles exhibited a uniform spherical shape and a particle size of 120–220 nm, whereas BSA nanoparticles had a particle size of approximately 10 nm, indicating that BSA combined successfully with IR-817. In addition, the particle size after BSA encapsulation of IR-817 is the optimal particle size for achieving EPR effect in tumor issue.[53] Although uptake by the reticuloendothelial system (RES) is inevitable as with small-molecule fluorescent probes, nanoprobes can be rapidly eliminated from normal tissues/organs via the kidney and can still be passively targeted to tumor with high concentration distribution at the tumor site via the EPR effect.[54] As shown in the mouse tumor-targeting imaging experiment, BSA@IR-817 showed non-specific accumulation except at the tumor site at 6 h, but it was metabolized out in large quantities around 12 h, and there was still strong fluorescence at the tumor site with only a slight decrease until 24 h.

NIR light is the most commonly used photosensitizer in phototherapy because it can interact with NIR radiation to stimulate certain changes in cells, and the NIR radiation has minimal interaction with biological components (such as water, collagen, and melanin) despite its deep penetration.[55] Due to these characteristics, NIR therapy is more selective for tumor areas, as only the photosensitizers that accumulate in the area can be activated by NIR light, thereby minimizing damage to healthy tissue. During the preliminary experiment, we determined that the temperature of IR-

817 dissolved in organic solvents (methanol and ethanol) would change significantly when exposed to laser 808, whereas the temperature of IR-817 dissolved in inorganic solvents (H_2O and PBS) would not change significantly. Correspondingly, we hypothesized that this was due to IR-817's poor solubility in water. Therefore, we were eager to further investigate its photothermal potential following the construction of BSA@IR-817 nanoparticles with improved in vivo and in vitro fluorescence effects. Excitingly, our results demonstrated that BSA@IR-817 could be heated to greater than 50 °C in vivo and in vitro when exposed to laser radiation of 808 (1 W/cm^2 for 5 min). Generally, a tumor site temperature of 50 °C or higher is optimal for hyperthermia; as such an increase in temperature will cause irreversible cell damage and necrosis of tumor cells.[56] This gives us hope for the photothermal treatment of tumors with BSA@IR-817. As anticipated, in a subcutaneously constructed melanoma mouse model, BSA@IR-817 exhibited a significant photothermal treatment effect under laser radiation, with a tumor inhibition rate of 99%, and no tumor recurrence was observed in the BSA@IR-817+Laser group several days after the end of treatment. Although BSA@IR-817 significantly reduced the toxicity of IR-817, it was discovered that at high concentrations, BSA@IR-817 could also inhibit melanoma growth both in vitro and in vivo. We hypothesized that BSA@IR-817 might initially enter the tumor site via the EPR effect and then lyse under the influence of the tumor microenvironment (TME) to liberate IR-817. As a result, the free IR-817 likely only exists at the tumor site to exert its antitumor effect, which is likely why BSA@IR-817 without laser irradiation has some antitumor effects but is extremely biosafe. However, this effect is limited and could possibly be enhanced by increasing the BSA@IR-817 concentration, but the resulting toxic side effects cannot be completely disregarded. Consequently, the use of an exogenous laser to irradiate a reasonable dose of BSA@IR-817 for photothermal treatment is currently the optimal method for enhancing the utility of IR-817.

Obviously, our study had limitations, such as whether BSA@IR-817 would release IR-817 only after entering the tumor site, as we hypothesized, and the precise mechanism by which it enters cells. In addition, the potential molecular mechanism underlying BSA@IR-817 photothermal therapy has only been preliminarily explored. And from the perspective of photothermal stability, the advantage of BSA@IR-817 is not outstanding, it is necessary to continue to explore better methods to improve the stability. Therefore, additional experiments are required to confirm these questions. However, the vast potential of BSA@IR-817 in photothermal therapy cannot be denied.

Conclusion

In conclusion, by interacting BSA with the near-infrared dye IR-817, we were able to construct BSA@IR-817 nanoparticles with the potential for targeted imaging and photothermal therapy in melanoma. We determined the optimal concentration and ratio for BSA and IR-817 binding as part of a reasonable screening procedure for BSA@IR-817. According to the characterization of BSA@IR-817 nanoparticles, BSA and IR-817 were found to be capable of forming nanoparticles with uniform size and stable structure. In addition, compared to IR-817, BSA@IR-817 had superior near-infrared fluorescence imaging capability, tumor site retention capability, and excellent in vitro and in vivo biocompatibility. Despite the fact that BSA significantly diminished IR-817's toxicity, IR-817's absorption wavelength became longer. Under laser 808 irradiation, this characteristic caused BSA@IR-817 to convert more of its light energy into heat energy. Additionally, a rise in temperature above 50 °C, was sufficient to kill tumor cells. In mice subcutaneously inoculated with B16-F10 melanoma, the thermal ablation effect of BSA@IR-817 on the tumor was up to 99%, demonstrating the effective photothermal therapeutic ability of BSA@IR-817. Thus, our study confirmed the superior imaging and photothermal treatment effects of BSA@IR-817 on melanoma, providing a novel method to enhance the curative efficacy of melanoma treatment.

Abbreviations

BSA, Bovine serum albumin; HSA, Human serum albumin; DLS, Dynamic light scattering; SEM, Scanning electron microscopy; PTAs, Photothermal transduction agents; NIR, Near-infrared; ICG, Indocyanine green; FDA, Food and Drug Administration; OATPs, Organic anion transporting polypeptides; ACQ, Aggregation caused quench; EPR, Permeability and retention; FBS, Fetal bovine serum; MTT, 3-(4,5-diMethylthialzol-2-yl)-2,5-diphe-nyltetrazolium bromide; CC-3, Cleaved caspase-3; SEM, Scanning electron microscopy; PI, Propidium iodide; H&E, Hematoxylin and eosin; PCE, photothermal conversion efficiency; RES, reticuloendothelial system; TME, The tumor microenvironment.

Data Sharing Statement

The datasets used and analyzed during the current study are available from the corresponding author on reasonable request.

Acknowledgments

Jianv Wang and Hongye Liao are co-first authors for this study. We thank Figdraw (www.Figdraw.com, accessed data: 21 May 2023) for the assistance in creating Scheme 1. We also thank Bullet Edits Limited for the linguistic editing and proofreading of the manuscript.

Funding

This work was supported by the National Natural Science Foundation of China (grant number: 82003716), Sichuan Science and Technology Program (2022YFS0631, 2022YFS0635), Luzhou Science and Technology Projects (2021-JYJ -48, 2022-JYJ-141), Innovation Team and Talents Cultivation Program of National Administration of Traditional Chinese Medicine (Number: ZYYCXTD-C-202207), Southwest Medical University School-level Project Fund (2021ZKMS049, 2022ZD011).

Disclosure

The authors declare that they have no known competing financial interests or personal relationships that could have appeared to influence the work reported in this paper.

References

1. Guo W, Wang H, Li C. Signal pathways of melanoma and targeted therapy. *Signal Transduct Target Ther*. 2021;6(1):424. doi:10.1038/s41392-021-00827-6
2. Hsu CH, Lee KJ, Chiu YH, et al. The lysosome in malignant melanoma: biology, function and therapeutic applications. *Cells*. 2022;11(9):1492. doi:10.3390/cells11091492
3. Wagstaff W, Mwamba RN, Grullon K, et al. Melanoma: molecular genetics, metastasis, targeted therapies, immunotherapies, and therapeutic resistance. *Genes Dis*. 2022;9(6):1608–1623. doi:10.1016/j.gendis.2022.04.004
4. Long GV, Menzies AM, Scolyer RA. Neoadjuvant checkpoint immunotherapy and melanoma: the time is now. *J Clin Oncol*. 2023;O2202575.
5. Serrati S, Guida M, Di Fonte R, et al. Circulating extracellular vesicles expressing PD1 and PD-L1 predict response and mediate resistance to checkpoint inhibitors immunotherapy in metastatic melanoma. *Mol Cancer*. 2022;21(1):20. doi:10.1186/s12943-021-01490-9
6. Nikolaou M, Pavlopoulou A, Georgakilas AG, Kyrodimos E. The challenge of drug resistance in cancer treatment: a current overview. *Clin Exp Metastasis*. 2018;35(4):309–318. doi:10.1007/s10585-018-9903-0
7. Kalal BS, Upadhya D, Pai VR. Chemotherapy resistance mechanisms in advanced skin cancer. *Oncol Rev*. 2017;11(1):326. doi:10.4081/oncol.2017.326
8. Bukowski K, Kciuk M, Kontek R. Mechanisms of multidrug resistance in cancer chemotherapy. *Int J Mol Sci*. 2020;21(9):3233. doi:10.3390/ijms21093233
9. Liu Y, Bhattarai P, Dai Z, Chen X. Photothermal therapy and photoacoustic imaging via nanotheranostics in fighting cancer. *Chem Soc Rev*. 2019;48(7):2053–2108. doi:10.1039/c8cs00618k
10. Zhang L, Liu Y, Huang H, et al. Multifunctional nanotheranostics for near infrared optical imaging-guided treatment of brain tumors. *Adv Drug Deliv Rev*. 2022;190:114536. doi:10.1016/j.addr.2022.114536
11. Li C, Cheng Y, Li D, et al. Antitumor applications of photothermal agents and photothermal synergistic therapies. *Int J Mol Sci*. 2022;23(14):56.
12. Qi X, Huang Y, You S, et al. Engineering robust ag-decorated polydopamine nano-photothermal platforms to combat bacterial infection and prompt wound healing. *Adv Sci*. 2022;9(11):e2106015. doi:10.1002/advs.202106015
13. Li C, Xu Y, Tu L, et al. Rationally designed Ru(ii)-metallacycle chemo-phototheranostic that emits beyond 1000 nm. *Chem Sci*. 2022;13(22):6541–6549. doi:10.1039/D2SC01518H
14. Zhang X, He Q, Sun J, et al. Near-Infrared-Enpowered Nanomotor-Mediated Targeted Chemotherapy and Mitochondrial Phototherapy to Boost Systematic Antitumor Immunity. *Adv Healthc Mater*. 2022;11(14):e2200255. doi:10.1002/adhm.202200255
15. Xu Y, Li C, Ma X, et al. Long wavelength-emissive Ru(II) metallacycle-based photosensitizer assisting in vivo bacterial diagnosis and antibacterial treatment. *Proc Natl Acad Sci U S A*. 2022;119(32):e2209904119. doi:10.1073/pnas.2209904119
16. Xu Y, Li C, An J, et al. Construction of a 980 nm laser-activated Pt(II) metallacycle nanosystem for efficient and safe photo-induced bacteria sterilization. *Sci China Chem*. 2023;66:155–163. doi:10.1007/s11426-022-1440-2
17. Egloff-Juras C, Bezdetnaya L, Dolivet G, Lassalle HP. NIR fluorescence-guided tumor surgery: new strategies for the use of indocyanine green. *Int J Nanomedicine*. 2019;14:7823–7838. doi:10.2147/IJN.S207486
18. Wang J, Jia J, He Q, et al. A novel multifunctional mitochondrion-targeting NIR fluorophore probe inhibits tumour proliferation and metastasis through the PPARγ/ROS/β-catenin pathway. *Eur J Med Chem*. 2023;258:115435. doi:10.1016/j.ejmech.2023.115435
19. Wang H, Li X, Tse BW, et al. Indocyanine green-incorporating nanoparticles for cancer theranostics. *Theranostics*. 2018;8(5):1227–1242. doi:10.7150/thno.22872

20. Song J, Ye H, Jiang S, Yang Y, Li X. An acid response ir780-based targeted nanoparticle for intraoperative near-infrared fluorescence imaging of ovarian cancer. *Int J Nanomedicine*. 2022;17:4961–4974. doi:10.2147/IJN.S375145
21. Li X, Lovell JF, Yoon J, Chen X. Clinical development and potential of photothermal and photodynamic therapies for cancer. *Nat Rev Clin Oncol*. 2020;17(11):657–674. doi:10.1038/s41571-020-0410-2
22. Tan X, Luo S, Wang D, Su Y, Cheng T, Shi C. A NIR heptamethine dye with intrinsic cancer targeting, imaging and photosensitizing properties. *Biomaterials*. 2012;33(7):2230–2239. doi:10.1016/j.biomaterials.2011.11.081
23. Ma X, Shi L, Zhang B, Liu L, Fu Y, Zhang X. Recent advances in bioprobes and biolabels based on cyanine dyes. *Anal Bioanal Chem*. 2022;414(16):4551–4573. doi:10.1007/s00216-022-03995-8
24. Zhang L, Jia H, Liu X, et al. Heptamethine Cyanine-Based Application for Cancer Theranostics. *Front Pharmacol*. 2021;12:764654. doi:10.3389/fphar.2021.764654
25. Lim W, Byun JY, Jo G, Kim EJ, Park MH, Hyun H. Molecular Tuning of IR-786 for Improved Tumor Imaging and Photothermal Therapy. *Pharmaceutics*. 2022;14(3):676. doi:10.3390/pharmaceutics14030676
26. Sun C, Wang J, Xia T, et al. Mitochondrion-Targeted NIR Therapeutic Agent Suppresses Melanoma by Inducing Apoptosis and Cell Cycle Arrest via E2F/Cyclin/CDK Pathway. *Pharmaceuticals*. 2022;15(12):1589. doi:10.3390/ph15121589
27. Shen X, Liu X, Li T, et al. Recent Advancements in Serum Albumin-Based Nanovehicles Toward Potential Cancer Diagnosis and Therapy. *Front Chem*. 2021;9:746646. doi:10.3389/fchem.2021.746646
28. Sleep D. Albumin and its application in drug delivery. *Expert Opin Drug Deliv*. 2015;12(5):793–812. doi:10.1517/17425247.2015.993313
29. Chung H, Park JY, Kim K, et al. Circulation Time-Optimized Albumin Nanoplatform for Quantitative Visualization of Lung Metastasis via Targeting of Macrophages. *ACS Nano*. 2022;16(8):12262–12275. doi:10.1021/acsnano.2c03075
30. Thavornpradit S, Usama SM, Lin CM, Burgess K. Protein labelling and albumin binding characteristics of the near-IR Cy7 fluorophore, QuatCy. *Org Biomol Chem*. 2019;17(30):7150–7154. doi:10.1039/C9OB01184F
31. Tian R, Zeng Q, Zhu S, et al. Albumin-chaperoned cyanine dye yields superbright NIR-II fluorophore with enhanced pharmacokinetics. *Sci Adv*. 2019;5(9):w672. doi:10.1126/sciadv.aaw0672
32. Jo G, Kim EJ, Hyun H. Enhanced Tumor Uptake and Retention of Cyanine Dye-Albumin Complex for Tumor-Targeted Imaging and Phototherapy. *Int J Mol Sci*. 2023;24(1):862. doi:10.3390/ijms24010862
33. An F, Yang Z, Zheng M, et al. Rationally assembled albumin/indocyanine green nanocomplex for enhanced tumor imaging to guide photothermal therapy. *J Nanobiotechnology*. 2020;18(1):49. doi:10.1186/s12951-020-00603-8
34. Jang HJ, Song MG, Park CR, et al. Imaging of Indocyanine Green-Human Serum Albumin (ICG-HSA) Complex in Secreted Protein Acidic and Rich in Cysteine (SPARC)-Expressing Glioblastoma. *Int J Mol Sci*. 2023;24(1):850. doi:10.3390/ijms24010850
35. Du B, Qu C, Qian K, Ren Y, Li Y. An IR820 Dye–Protein Complex for Second Near-Infrared Window and Photoacoustic Imaging. *Adv Optical Mater*. 2019.
36. Chen Q, Wang C, Zhan Z, et al. Near-infrared dye bound albumin with separated imaging and therapy wavelength channels for imaging-guided photothermal therapy. *Biomaterials*. 2014;35(28):8206–8214. doi:10.1016/j.biomaterials.2014.06.013
37. An FF, Zhang XH. Strategies for Preparing Albumin-based Nanoparticles for Multifunctional Bioimaging and Drug Delivery. *Theranostics*. 2017;7(15):3667–3689. doi:10.7150/thno.19365
38. Kalyane D, Raval N, Maheshwari R, Tambe V, Kalia K, Tekade RK. Employment of enhanced permeability and retention effect (EPR): nanoparticle-based precision tools for targeting of therapeutic and diagnostic agent in cancer. *Mater Sci Eng C Mater Biol Appl*. 2019;98:1252–1276. doi:10.1016/j.msec.2019.01.066
39. Yu Y, Tang D, Liu C, et al. Biodegradable Polymer with Effective Near-Infrared-II Absorption as a Photothermal Agent for Deep Tumor Therapy. *Adv Mater*. 2022;34(4):e2105976. doi:10.1002/adma.202105976
40. Yang Y, Hu D, Lu Y, et al. Tumor-targeted/reduction-triggered composite multifunctional nanoparticles for breast cancer chemo-photothermal combinational therapy. *Acta Pharm Sin B*. 2022;12(6):2710–2730. doi:10.1016/j.apsb.2021.08.021
41. Zhao X, Zhao H, Wang S, et al. A Tumor-Targeting Near-Infrared Heptamethine Cyanine Photosensitizer with Twisted Molecular Structure for Enhanced Imaging-Guided Cancer Phototherapy. *J Am Chem Soc*. 2021;143(49):20828–20836. doi:10.1021/jacs.1c09155
42. Schneider A, Zhang Y, Zhang M, et al. Membrane-associated PGE synthase-1 (mPGES-1) is coexpressed with both COX-1 and COX-2 in the kidney. *Kidney Int*. 2004;65(4):1205–1213. doi:10.1111/j.1523-1755.2004.00493.x
43. Xu L, Wang SB, Xu C, et al. Multifunctional Albumin-Based Delivery System Generated by Programmed Assembly for Tumor-Targeted Multimodal Therapy and Imaging. *ACS Appl Mater Interfaces*. 2019;11(42):38385–38394. doi:10.1021/acsami.9b11263
44. Canovas C, Bellaye PS, Moreau M, Romieu A, Denat F, Goncalves V. Site-specific near-infrared fluorescent labelling of proteins on cysteine residues with meso-chloro-substituted heptamethine cyanine dyes. *Org Biomol Chem*. 2018;16(45):8831–8836. doi:10.1039/C8OB02646G
45. Usama SM, Park GK, Nomura S, Baek Y, Choi HS, Burgess K. Role of Albumin in Accumulation and Persistence of Tumor-Seeking Cyanine Dyes. *Bioconjug Chem*. 2020;31(2):248–259. doi:10.1021/acs.bioconjchem.9b00771
46. Xu J, Han T, Wang Y, et al. Ultrabright Renal-Clearable Cyanine-Protein Nanoprobes for High-Quality NIR-II Angiography and Lymphography. *Nano Lett*. 2022;22(19):7965–7975. doi:10.1021/acs.nanolett.2c03311
47. Bai L, Hu Z, Han T, et al. Super-stable cyanine@albumin fluorophore for enhanced NIR-II bioimaging. *Theranostics*. 2022;12(10):4536–4547. doi:10.7150/thno.71443
48. Shi Y, van der Meel R, Chen X, Lammers T. The EPR effect and beyond: strategies to improve tumor targeting and cancer nanomedicine treatment efficacy. *Theranostics*. 2020;10(17):7921–7924. doi:10.7150/thno.49577
49. Jain AK, Thareja S. In vitro and in vivo characterization of pharmaceutical nanocarriers used for drug delivery. *Artif Cells Nanomed Biotechnol*. 2019;47(1):524–539. doi:10.1080/21691401.2018.1561457
50. Niu G, Zhang R, Gu Y, et al. Highly photostable two-photon NIR AIEgens with tunable organelle specificity and deep tissue penetration. *Biomaterials*. 2019;208:72–82. doi:10.1016/j.biomaterials.2019.04.002
51. Ma R, Alifu N, Du Z, et al. Indocyanine Green-Based Theranostic Nanoplatform for NIR Fluorescence Image-Guided Chemo/Photothermal Therapy of Cervical Cancer. *Int J Nanomedicine*. 2021;16:4847–4861. doi:10.2147/IJN.S318678
52. Chen Q, Liu Z. Albumin Carriers for Cancer Theranostics: a Conventional Platform with New Promise. *Adv Mater*. 2016;28(47):10557–10566. doi:10.1002/adma.201600038

53. Deshantri AK, Varela MA, Ecker V, et al. Nanomedicines for the treatment of hematological malignancies. *J Control Release*. 2018;287:194–215. doi:10.1016/j.jconrel.2018.08.034
54. Yu M, Zheng J. Clearance Pathways and Tumor Targeting of Imaging Nanoparticles. *ACS Nano*. 2015;9(7):6655–6674. doi:10.1021/acsnano.5b01320
55. Alves CG, Lima-Sousa R, de Melo-Diogo D, Louro RO, Correia IJ. IR780 based nanomaterials for cancer imaging and photothermal, photodynamic and combinatorial therapies. *Int J Pharm*. 2018;542(1–2):164–175.
56. de Melo-Diogo D, Pais-Silva C, Dias DR, Moreira AF, Correia IJ. Strategies to Improve Cancer Photothermal Therapy Mediated by Nanomaterials. *Adv Healthc Mater*. 2017;6(10):1700073. doi:10.1002/adhm.201700073